Improving the shear design of steel-bar reinforced ultra high performance fibre reinforced concrete beams using mesoscale modelling

Zhang, Y., Yang, Z., Zhang, H., Tsang, N. & Zhang, X.

DOI 10.1177/13694332221137174
ISSN 1369-4332

Publisher: SAGE Publications

Improving the shear design of steel-bar reinforced ultra high performance fibre reinforced concrete beams using mesoscale modelling

Yuming Zhang[a,b], Zhenjun Yang[a*], Hui Zhang[c], Neil Tsang[b], Xiaoxian Zhang[a,d]

[a] Hubei Key Laboratory of Geotechnical and Structural Safety, School of Civil Engineering, Wuhan University, 430072, China; [b] Institute for Future Transport and Cities, Coventry University, Coventry, CV1 5FB, UK; [c] School of Mechanical Engineering, The North University of China, 030051, China; [d] Rothamsted Research, Harpenden, AL5 2JQ, UK

Abstract:

Understanding the failure mechanisms of steel-bar reinforced ultra high performance fibre reinforced concrete (UHPFRC) beams is crucial to improving their design but challenging because of the contrast between beam size and fibre size. We develop a 2D mesoscale finite element model with the fibres explicitly resolved to bridge this gap by simulating the damaging and fracturing processes of the beams. To make fibre distribution in the model mechanically representative, we propose a method to project the fibres from 3D to 2D. The continuum damaged plasticity model is used as the constitutive law for the UHPC matrix, and the zero-thickness cohesive elements with softening constitutive law are used to model the nonlinear bond-slip behaviour of the fibre- and bar-matrix interfaces. The models are validated against experimental data obtained from 3 and 4-point loading tests by comparing the simulated and measured fracturing processes, crack patterns and the load-displacement curves. The validated models are then used to analyse the sensitivity of the shear strength of the beams to fibre content, shear span-to-depth ratio, as well as shear and longitudinal reinforcement ratios in the beam, from which a shear strength equation is proposed to improve the design of reinforced UHPFRC beams. The improvement of the new equation over the AFGC equation is demonstrated against experimental data measured from 32 beams with various material properties.

***Corresponding author. *Email*: zhjyang@whu.edu.cn (Z Yang)**

Key words: *UHPFRC; Meso-scale Finite Element Model; Damage Plasticity Model; Cohesive Elements; Parametric Analysis; Shear Design.*

1. Introduction

The ultra high performance steel fibre reinforced concrete (UHPFRC) is a comparatively new fibre reinforced concrete (FRC). Its superior mechanical properties, including high compressive strength (>150MPa), tensile strength (>8MPa), fracture energy (40kJ/m^2) and durability, make it potential to replace the conventional reinforcing steel bars in reinforced concrete (RC) structures, such as thin slabs and shells (Serna et al., 2009; Alberti et al., 2014; Pujadas et al., 2014). It has hence attracted increased interest from both researchers and engineers over the past decades (Richard and Cheyrezy, 1995). However, because steel-bar reinforced and unreinforced UHPFRC structures are 5-10 times more expensive than normal strength concrete (NSC), their practical applications in engineering projects are still limited (Aitcin, 2000; Voort et al., 2008; Russell and Graybeal, 2013). Understanding the mechanisms underlying the change in shear strength of UHPFRC structures with fibre content and other material properties is essential to reducing their costs and facilitating their application.

Modulated by casting procedure, the orientation and distribution of steel fibres in UHPFRC structures are opaque and spatially random (Barnett et al., 2010; Boulekbache et al., 2010; Deeb et al., 2014), while their consequence for structural performance remains elusive, despite decade of studies (Yang et al., 2010; Bertram and Hegger, 2012; Baby et al., 2013; Qing et al., 2019). Tomography techniques such as X-ray computed tomography (CT) can visualise the components in UHPFRC at resolutions as fine as a few microns (Zhan and Meschke, 2016; Qsymah et al., 2017; Yang et al., 2020; Zhang et al., 2021), but their high cost and the tradeoff between spatial resolution and the size of samples for scanning means that CT is not applicable to identify fibres in large UHPFRC beams.

Traditional FRC and UHPFRC models for macroscale represent the heterogeneous micro-features and their impact implicitly using constitutive laws, such as the damaged plasticity model (Mahmud et al., 2013), the microplane model (Liu et al., 2009), the failure surface model (Özcan et al., 2009), and the stress transfer-based model (Lu et al., 2017). Parameters in these models are usually determined from laboratory tests. While the macroscale models can predict structure failure, they are unable to unveil whether the failure is caused by individual fibres, bars, matrix, material interfaces, or their combination. Mesoscale modelling with these micro-features explicitly resolved can bridge this gap and has the potential to improve UHPFRC design (Zhang et al., 2022).

Various meso-scale models have been developed over the past decades (Laranjeira et al., 2010; Ellis et al., 2014; Jia et al., 2015; Zhang and Yu, 2016), but most of them are to simulate single fibre pull-out tests (SFPTs) or calculate bulk mechanical properties of specimens. The random fibre distribution in these models is either numerically generated or obtained from CT images (Qsymah et al., 2017; Zhang et al., 2021), with the fibre-matrix interaction described by the tensile stress-strain constitutive laws estimated from the load-slip curves from SFPT tests (Pros et al., 2012; Kang et al., 2014). One shortcoming of these methods is that the constitutive laws are empirical and unable to differentiate the impacts of fibre elongation and bond-slip on the fibre-matrix interfaces. They are thus inadequate to describe the stress on individual fibres (Cunha et al., 2012; Yu et al., 2016). As an improvement, Zhang et al. (2018) developed a discrete-continuum model with the fibre-matrix interfacial debonding described by softening cohesive elements.

There have been some experimental studies on shear capacity and shear behaviour of UHPFRC beams and girders without shear reinforcement (Voo et al., 2010; Baby et al., 2014). In general, however, there is still a lack of accurate understanding of how the shear behaviour of bar-reinforced UHPFRC beams varies with design parameters, such as fibre content and orientation, beam slenderness, shear reinforcement ratio, longitudinal reinforcement ratio and prestressing level (Baby et al., 2013). As a result, the design of UHPFRC beams usually uses a high safety margin (Graybeal, 2006; Florent et al., 2013). Understanding the effects of individual design parameters on the shear behaviour and failure mechanisms of UHPFRC beams is therefore essential to improve their design.

The primary objective of this paper is to propose a mesoscale model to help improve design of steel bar-reinforced UHPFRC beams. Fibre distribution in UHPFRC beams is three-dimensional, however, because of the contrast between beam size and fibre size, directly modelling 3D beams with all fibres explicitly resolved is computationally infeasible. We hence model the 3D beam by a 2D plane and propose a method to project the fibres from 3D to 2D to ensure that the results simulated from the 2D model are mechanically equivalent. The 2D models are tested against experimental data measured from real-size structural members. They are then used to analyse the sensitivity of shear strength of the beams to design parameters including fibre content, shear span-to-depth ratio, shear reinforcement ratio, and longitudinal reinforcement ratio, from which an equation is proposed to improve the shear design of UHPFRC beams, with or without the stirrups, under 3- and 4-point bending. This equation is applied to experimental data obtained from 32 beam tests with different material properties, and its improvement is demonstrated against the method recommended by the AFGC code (2002).

2. Finite element modelling

2.1 Determination of fibre content for the 2D models

The fibre distribution in the 2D mesoscale FE models is calculated by projecting the fibres in 3D into a 2D plane, with the effects of out-of-plane distributed fibres, matrix size and fibre volume fraction taken into account. We firstly generate N fibres randomly distributed in a cube of size L_m using a Matlab code, with the fibre length and fibre volume fraction represented by L_f and A_f, respectively (Figure 1a). Each fibre is then projected into a 2D plane (Figures 1b-c), based on that only fibres whose cross-sections and contacting interfaces are parallel to the 2D plane can carry load. This is a conservative approach for structural design as it neglects the out-of-thickness. The total length of all fibres in the 2D plane is represented by L_{2D}, and the projecting ratio is defined as $K_{2D}=L_{2D}/(N{\cdot}L_f)$. To investigate the effect of out-of-plane thickness in the 2D models, we generate 9000 samples with the fibre volume content varying from 0.2 to 3.0% and sample size (L_m) from 1 to 15L_f. For each combination of sample size and fibre content, there are 50 samples with the random fibre distribution in them independent of each other. Figure 2a shows the change in K_{2D} and its mean obtained from 750 samples with the normalized sample size (by L_f) for A_f=1.0%, and Figure 2b shows the change in the mean K_{2D} of the 9000 samples with the normalized sample size for different A_f. It is evident that K_{2D} asymptotes to 0.631 when $L_m \geq 5L_f$, regardless of A_f, indicating that the minimum sample size to avoid out-of-plane thickness effect in the 2D model is 5 times the fibre length. The associated area fraction in the 2D model is approximately 0.631A_f. To avoid non-conforming elements and meshing difficulty when the projected fibres are not long enough in the 2D plane, the number of projected fibres is modified to N_{2D} based on the area fraction of fibre 0.631A_f and the fibre length L_f, as illustrated in Figure 1d.

2.2 Generation of FE meshes

The reinforced UHPFRC beams consist of UHPC matrix, steel fibres, steel bars, fibre-matrix and bar-matrix interfaces. The matrix is discretized by the four-node isoparametric elements (CPS4R in Abaqus). The steel bars, stirrups and randomly distributed fibres are modelled by the two-node Timoshenko beam elements (B21), with their bending resistance represented by the elastoplastic constitutive laws. The fibre diameter is not explicitly simulated but input as a parameter to compute the elemental stiffness. The zero-thickness cohesive elements (COH2D4 in Abaqus) are inserted between the fibres/steel bars and the matrix to represent their interfaces in a way illustrated in Figure 3a, where the fibres and steel bars are treated as boundaries of the matrix in mesh generation. The fibres, steel bars and interfaces are defined by double layers of nodes, and they "float" over the UHPC matrix (Figure 3b) to avoid fine mesh localization in the matrix adjacent the thin fibres, which would occur if directly loading the fibre nodes on the matrix plane. Visually, the projected fibres could intersect in the 2D plane as shown illustratively in Figure 3b. Computationally, however, such an intersection does not have any mechanical impact as the nodes of different fibres at the intersection are differentiated using different node numbers, i.e., N1 of fibre 1, N2 of fibre 2 and N3 of the matrix. Such fibres do not intersect with each other in the modelling. Displacement constraints are applied to the nodes of these elements to deform the 2D plane, and the fibre and bar elements in the model can only move longitudinally along their axes as illustrated in Figure 3b.

2.3 Constitutive laws for matrix and fibre/bar-matrix interfaces

The widely used concrete damaged plasticity (CDP) model in Abaqus for damage and fracture of concrete-like materials is employed to model the nonlinear constitutive behaviour of the UHPC matrix (Earij et al., 2017; Mahmud et al., 2013; Huang et al., 2015; Huang et al., 2016). It defines the compressive hardening, tensile softening, damage initiation and evolution. The pre-peak stress-strain relationships between compression and tension are assumed to be linearly elastic, while the post-peak softening compressive behaviour is described by the model of Guo (2004):

$$\frac{\sigma_c}{f_c} = \frac{\frac{\varepsilon}{\varepsilon_c}}{\alpha\left(\frac{\varepsilon}{\varepsilon_c}-1\right)^2+\frac{\varepsilon}{\varepsilon_c}} \tag{1}$$

where σ_c and ε are the compressive stress and strain respectively, ε_c is the compressive strain at the ultimate strength, α is an experimental coefficient assumed to depend on the compressive strength (f_c) in α=0.157$f_c^{0.785}$-0.905.

The tensile softening behaviour of the UHPC matrix is described by the following traction (σ_t)-crack opening displacement (w) curve (Hordijk, 1992), to minimize the impact of mesh:

$$\frac{\sigma_t}{f_t} = \left[1+\left(3\frac{w}{w_0}\right)^3\right]e^{\left(-6.93\frac{w}{w_0}\right)} - 10\frac{w}{w_0}e^{(-6.93)} \tag{2}$$

where w_0 is the crack opening displacement when the traction approaches to zero, calculated by w_0=5.4 G_f/f_t in which G_f and f_t are the fracture energy and tensile strength, respectively.

The compression damage index d_c and the tension damage index d_t in the CDP model are estimated by the following equations (Birtel and Mark, 2006) assuming the compressive and tensile plastic strains are proportional to the inelastic compression and tension strains respectively, with the proportionalities being constant:

$$d_c = 1 - \frac{\sigma_c {E_c}^{-1}}{\varepsilon_c^{pl}\left(\frac{1}{b_c}-1\right)+\sigma_c {E_c}^{-1}} \tag{3}$$

$$d_t = 1 - \frac{\sigma_t {E_t}^{-1}}{\varepsilon_t^{pl}\left(\frac{1}{b_t}-1\right)+\sigma_t {E_t}^{-1}} \tag{4}$$

where σ_c and σ_t are the compressive and tensile stresses respectively, E_c is the elastic modulus of the matrix, ε_c^{pl} and ε_t^{pl} are the compressive and tensile plastic strains respectively, b_c and b_t

are constant taken as 0.7 and 0.1 respectively. Other five parameters in the CDP model are the dilation angle, the flow potential eccentricity, the ratio of initial equibiaxial compressive yield stress to initial uniaxial compressive yield stress, the ratio of the second stress invariant on the tensile meridian to that on the compressive meridian, and the viscosity parameter. Their values are taken as 33°, 0.1, 1.16, 0.667 and 0.005, respectively.

The shear traction (t_s)-slip (δ_s) curve shown in Figure 4 is used as the constitutive law for the cohesive elements to simulate the softening bond-slip behaviour of both fibre-matrix and bar-matrix interfaces. The maximum normal traction t_{n0} is assumed to be ten times the shear traction t_{s0} to ensure that only interfacial shear slip (i.e., no opening) is allowed. Damage initiation emerges when the shear traction reaches t_{s0}. The following linear function is used as the criterion to determine the damage evolution in the cohesive elements:

$$D = \frac{\delta_s^f(\delta_s - \delta_s^0)}{\delta_s(\delta_s^f - \delta_s^0)} \quad (5)$$

where δ_s is the slip, δ_s^0 is the slip at t_{s0}, and δ_s^f is the maximum slip.

3. Numerical examples, results and discussion

Two beam examples with experimental data are modelled. After a number of trial-errors, the Abaqus/Explicit solver with a total time 0.05s and time increment 1×10^{-7}s is used in all simulations to ensure the quasi-static loading condition. The loading is applied by uniformly distributing displacements at the loading points. A PC with an Intel(R) Core i9-9900K CPU@3.60GHz is used for all simulations. A typical simulation takes 2 to 4 hours, depending on the degrees of freedom in the model.

3.1 Example 1: a UHPFRC beam reinforced with longitudinal steel bars

The simply supported reinforced UHPFRC beam tested by Lim and Hong (2016) under three-point bending is modelled first. The boundary conditions and geometries are shown in Figure 5. The beam has longitudinal steel reinforcements only, and the concrete cover is 30 mm. Half of the beam is modelled, considering the symmetry. The fibre volume fraction is 1.5%. After trials-errors, the interfacial bonding strength t_{s0} for the fibre-matrix and bar-matrix interfaces is 11MPa and 15MPa respectively, and the initial stiffness in the softening laws for the fibre-matrix and bar-matrix interfaces is 3×10^5MPa/mm and 2×10^5MPa/mm respectively. Other material properties are determined from the experiments (Lim and Hong, 2016), and their values are given in Table 1. In all simulations, the fibre-matrix and bar-matrix interfaces are assumed to have the same density as the matrix.

3.1.1 Mesh sensitivity

Mesh sensitivity is analysed with the elemental size being 0.75mm, 1mm and 2mm. As an illustration, Figures 6a-c compare the three meshes for a beam having the same fibre distribution. The final crack patterns simulated from the three meshes using a tensile damage index DAMAGET≥0.9 are shown in Figures 6d-f, with the simulated macro-cracks represented by red matrix elements. For comparison, the crack pattern measured from the experiment is shown in Figure 6g. As expected, finer meshes result in narrower cracks, typical for the crack band concept used in the CDP model. The simulated load (F)-displacement (δ) curves from the three meshes are shown in Figure 7, along with the experimental results. Overall, they agree well in terms of both load-displacement curves and final crack patterns. Considering computational accuracy and efficiency, the mesh size 1mm is used in the following analysis of the impact of fibres for this example.

3.1.2 Load-displacement curves and cracking processes

We simulated four random fibre distributions and showed their load-displacement curves in Figure 8. The simulated final crack patterns and load-displacement curves agree well with the experimental results. Figure 9 illustratively shows five deforming stages, corresponding to Points 1-5 on the load-displacement curve respectively, snapshotted from one simulation. Cracks do not appear in the elastic stage (Figure 9a). At the peak load (Figure 9b), a few flexural cracks, emanating from the beam, pass through the main bars first and then propagate towards the loading point. The damage occurs on the bar-matrix interfaces, indicating an interfacial slip. After the peak load, an increased number of flexural cracks develop along the bottom and then propagate towards the loading point until a crack approaches the right support after the main bars yield (Figure 9c). This crack pattern remains unchanged except the two diagonal cracks, which continue to widen (Figure 9d) until a crack appears on the top surface, followed by a sudden failure (Figure 9e). This is a typical shear diagonal failure mode for RC beams without shear links under three-point bending (Khuntisa et al., 1999; Yang and Chen, 2005).

3.2 Example 2: UHPFRC beams reinforced with longitudinal bars and stirrups

This example models the three UHPFRC beams reported in Bahij et al. (2017). They are reinforced by longitudinal bars and stirrups under four-point bending. The parameters for the three beams are: Beam-A (a/d=1.8, s=200mm), Beam-B (a/d=1.8, s=370mm), and Beam-C (a/d=2.6, s=370mm). Figure 10 shows illustratively the dimensions and boundary conditions of Beam-A. For all three beams, the volume fraction of steel fibre is 1.0%, the concrete cover is 35mm, the effective depth d is 182.5mm, the interfacial strength t_{s0} is 10MPa for the fibre-matrix interfaces and 15MPa for the bar-matrix interfaces, the initial stiffnesses in the softening laws for the fibre-matrix and bar-matrix interfaces are 3×10^5MPa/mm and 2×10^5MPa/mm, respectively. Other material properties are taken from Bahij et al. (2017) and their values are given in Table 2. For each beam, five samples with the random fibre distribution in them independent of each other are simulated.

Figure 11 shows the simulated shear load-midspan displacement curves for the three beams in comparison with experimental data (Bahij et al., 2017). As anticipated, the peak shear load decreases as the stirrup spacing or the shear span to effective depth ratio increases, typical for RC beams. An increase in s (or lower shear reinforcement ratio) or a/d makes the structural behaviour more brittle in terms of lower deflection at the same loading level and lower dissipated energy (the area under the curve). In addition, the same level of randomness in the fibre distribution appears to result in less scattered data in the more brittle beams (Figures 11b-c). Figure 12 shows an exemplary cracking process in Beam-A, typical compression-shear failure for RC beams when a/d is in the range of 1 to 3. Figures 12d and 13 show the final crack patterns (at δ=25.2mm) simulated for the three beams, in comparison with the experimental observation (Figures 12e and 13). Figure 14 shows several local cut-off regions from Beam-A (Figure 16d) to visualize fibre deformation and stresses, in which the matrix elements with DAMAGET≥0.6 are removed to highlight the fibres. In the figures, fibre bending and pull-out (Figure 14a), fibre yielding (Figure 14b), fibre bridging (Figure 14c) and steel bar yielding (Figure 14d) are all visible.

4. Using the meso-scale model to improve the shear design of UHPFRC beams

The close agreement between the simulated and measured crack patterns and load-displacement curves for beams with different material properties and under various bending conditions indicates that the 2D models capture the mechanisms underlying beam failures at material scale. They can thus be used to help design UHPFRC beams. Taking the reinforced UHPFRC beam in Example 2 as an example, we explain how the mesoscale model can improve the shear design, considering four key parameters, each varying widely to cover the values possibly used in application.

The values of the four parameters are: fibre volume fraction A_f (0.5%, 1.0%, 1.5% and 2.0%), the shear span-to-depth ratio *a/d* (1.0, 1.4, 1.8, 2.2, 2.6, 3.0 and 3.5), the shear reinforcement ratio ρ_{sv} (1.04%, 0.52%, 0.35% and 0.26%), and the main bar (or flexural) reinforcement ratio ρ (1.29%, 1.94%, 2.58% and 3.23%). The reference parameters are ρ_{sv}=0.28% (or s=370mm), A_f=1.0%, *a/d*=1.8 and ρ=1.94%, associated with Beam-B in Example 2. Overall, there are 16 combinations of parameters in the analyses. For each combination, 30 samples are randomly generated, with fibre distribution in them independent of each other. The shear strength calculated from the simulations is compared with that estimated from the design equation recommended by AFGC (AFGC, 2002), from which an improved equation is proposed.

4.1 The AFGC recommended shear strength equation for UHPFRC beams

The AFGC recommended design equation (AFGC, 2002) for shear strength of reinforced UHPFRC beams is:

$$V_d = V_c + V_{fb} + V_s \tag{6}$$

where V_c, V_{fb} and V_s are shear strength of the UHPC matrix, stirrups, and steel fibres, respectively. V_c is calculated from

$$V_c = 0.14\sqrt{f_c}bd \tag{7}$$

where b and d are the width and effective depth of the beam, respectively.

V_s is calculated from

$$V_s = 0.9d\frac{A_v}{s}\frac{f_{yv}}{\gamma_s}\cot(\theta) \tag{8}$$

where A_v, f_{yv} and γ_s are the cross-sectional area of the stirrups (two legs in the models), the yield strength, and the partial safety factor (taken as 1.3), respectively; θ is the angle between the principal compression stress and the beam axis, and the recommended minimum θ is 30°.

V_{fb} is calculated from

$$V_{fb} = \frac{A\sigma_{Rd,f}}{K\,\gamma_{bf}\tan(\theta)} \tag{9}$$

where A is approximated by 0.9bd for beams with rectangular section; K is the fibre orientation and distribution coefficient, assumed to be 1.25 for all loading conditions; γ_{bf} is the partial safety factor taken as 1.3; $\sigma_{Rd,f}$ is the mean of the post-cracking strength calculated as follows based on the tensile stress-displacement curves of UHPFRC

$$\sigma_{Rd,f} = \frac{1}{w_{max}}\int_0^{w_{max}} \sigma_f(w)dw \tag{10}$$

where w_{max} is the maximum crack width (>0.3mm); $\sigma_f(w)$ is the relationship between tensile stress and crack opening displacement, derived from inverse analysis of notched beams under three-point bending. We used the mesoscale model to calculate the $\sigma_f(w)$ curve, from which $\sigma_{Rd,f}$ was estimated and used in Eq. 9 to calculate V_{fb}.

4.2 Effects of the fibre volume fraction

Figures 15a-d show the predicted shear load-midspan displacement curves calculated from the 30 samples with different A_f. As an example, the effects of sample number on peak shear load V_p (the predicted shear strength) and its standard deviation for A_f =1.0% are shown in Figure 15e and Figure 15f, respectively. It is clear that 30 samples are sufficient to obtain statistically convergent results. Figure 16a shows the mean shear load-midspan displacement curves of the 30 samples for different A_f, indicating that A_f affects both the shear strength V_p and the post-peak response (or ductility) significantly.

The variations in V_p and V_d calculated from Eq. 6 with A_f are shown in Figure 16b. V_p increases asymptotically as A_f increases, indicating the existence of an optimal fibre volume fraction for design. This is typical for reinforced UHPFRC beams (Bertram and Hegger, 2012; Baby et al., 2013). The difference between V_p and V_d is negligible when A_f is less than 1.0%, but it increases by 2.7% and 5.1% when A_f increases to 1.5% and 2.0%, respectively, indicating that the AFGC design equation underestimates the shear strength for A_f>1.0%. This underestimation can be corrected by multiplying V_d by a coefficient γ_f calculated as follows:

$$\gamma_f = 0.0725A_f + 0.935 \tag{11}$$

The accuracy of Eq. (11) is shown in Figure 16c (R^2=0.9929).

4.3 Effects of the shear span-to-depth ratio (*a/d*)

Figure 17a shows the mean shear load-midspan displacement curves calculated from the 30 samples for different *a/d*, as well as those in Figures 13a-b for *a/d*=1.8 and 2.6. When *a/d* increases from 1.0 to 2.6, V_p decreases sharply from 267.5kN to 105.7kN. A further increase in *a/d* beyond 2.6, however, does not lead to a noticeable change in V_p. This is consistent with experimental results of conventional RC beams and UHPFRC beams (Bertram and Hegger, 2012; Tadepalli et al., 2015).

The variations in V_p and V_d with *a/d* are shown in Figure 17b. V_p and V_d are close only when *a/d* is in the range of 1.8-2.6. Since the AFGC design equation does not explicitly consider the effects of *a/d*, it significantly underestimates the shear strength by 17.9% when *a/d*=1.0 and 12.1% when *a/d* is 3.0 and 3.5. Eurocode 2 accounts for the increase in the shear strength of RC beams when *a/d* is in the range of 0.5-2.0 by a multiplier $\beta=2d/a$ (2004). Applying this approach to the AFGC design equation, however, leads to large errors when *a/d* is low. Multiplying V_d by a coefficient γ_a calculated as follows can substantially improve the accuracy:

$$\gamma_a = 1.2176(a/d)^{-0.161} \tag{12}$$

The accuracy of Eq. (12) is shown in Figure 17c (R^2=0.9964).

4.4 Effects of the shear reinforcement ratio (ρ_{sv})

Figure 18a shows the mean load-midspan displacement curves calculated from the 30 samples for different ρ_{sv}. The variations in V_p and V_d with ρ_{sv} are shown in Figure 18b. They are virtually identical, indicating that the AFGC design equation describes the effect of stirrups well. When ρ_{sv} increases from 0.26% to 1.04%, the shear strength increases by 57.8% from 137.3kN to 216.7kN, indicating that, similar to conventional RC beams, the use of shear links is most effective to enhance the shear strength of UHPFRC beams.

4.5 Effects of the main steel-bar reinforcement ratio (ρ)

The dowel action refers to the resistance of flexural reinforcement to opening and slipping of the shear cracks. In the design of conventional RC beams, because of the low tensile strength of the concrete cover and the low bond strength of the steel bars-matrix interfaces, this resistance is insufficient and often omitted. SFRC materials have higher tensile strength and bonding, and the dowel actions of SFRC beams are thus much stronger (Sharma, 1986; Narayanan and Darwish, 1987; Kwak et al., 2002; Pourbaba et al., 2019). Previous study showed that the dowel action could contribute 10%-35% of the shear resistance of SFRC beams without stirrups (Zarrinpour and Chao, 2017).

Figure 19a shows the mean shear load-midspan displacement curves calculated from the 30 samples for different ρ. When ρ increases from 1.29% to 3.23%, V_p increases by 9.6% from 143.1kN to 156.8kN, because increasing ρ increases the flexural steel bars, thereby enhancing the dowel action. This is consistent with experimental results of steel-bar reinforced UHPFRC beams (Meda et al., 2012; Hasgul et al., 2018). Figure 19b shows the variations in V_p and V_d with ρ. Eq. (6) does not consider ρ and the errors of the shear strength estimated by it varies with ρ. When ρ is 3.23%, Eq. (6) underestimates the shear strength by 6%, while when ρ is 3.23%, it overestimates the strength by 3.21%. The overestimated shear strength is due to the negative effect of insufficient flexural reinforcement on shear strength and ductility, which results in stress concentration from the bars. This is consistent with the experimental results for SFRC and UHPFRC beams when ρ is low (Yang et al., 2010; Yoo and Yoon, 2015; Dancygier and Berkover, 2016; Hasgul et al., 2018; Turker et al. ,2019). Therefore, low flexural reinforcement ratio should be avoided in design.

The dowel action in RC beams is usually calculated analytically using concrete tensile strength (Taylor, 1969), because the concrete cover would fail via splitting when the acting dowel force is large. Based on our simulations, we add a term V_ρ calculated as follows to V_d to account for the contribution of the dowel action.

$$V_\rho = (0.8403\rho f_t - 0.0976)bd \tag{13}$$

The accuracy of Eq. (13) is shown in Figure 19c (R^2=0.9837):

4.6 The improved design equation

Based on the above parametric analyses, an improved design equation for shear strength of the steel-bar reinforced UHPFRC beams is proposed as follows:

$$V_d = \gamma_a\left(V_c + \gamma_f V_{fb} + V_\rho + V_s\right) \tag{14}$$

where γ_f, γ_a, and V_ρ are calculated by Eq. 11, Eq. 12 and Eq. 13 to account for the effects of A_f, a/d and ρ, respectively. To demonstrate the improvements of Eq. 14 over Eq. 6, we analysed the experimental results of 32 UHPFRC beams with various design parameters tested by 10 groups (Table 3). The shear strengths calculated from Eq. 6 and Eq. 14 are shown in Figure 20a and Figure 20b, respectively, along with the experimental results (V). It is manifest that Eq. (6) underestimates the shear strength, with the average V_d/V being 0.88 and the coefficient of variation being 12.93%. In contrast, the proposed equation significantly improves the accuracy, with the average V_d/V and the coefficient of variation being 1.03 and 3.41%, respectively.

5. Conclusions

Two-dimensional nonlinear meso-scale FE models have been developed to simulate failing processes of bar-reinforced UHPFRC beams, with the steel fibres and bars, and fibres/bars-matrix interfaces explicitly resolved. The main conclusions are:

(1) Validation against experimental data for two typical beams shows that the models accurately reproduce both failure patterns and load-displacement curves. The close agreement between them proves that the 2D models are efficient and adequate to analyse 3D beams, when the fibre area fraction in the 2D models is approximated by 63.1% of the fibre volume fraction in 3D and the out-of-plane thickness is at least 5 times the fibre length.

(2) All simulations show that the shear strength of typical bar-reinforced UHPFRC beam increases with the increase in fibre content, shear and flexural reinforcement ratios, but decreases with the increase in shear span-to-depth ratio.

(3) A new equation is proposed based on extensive mesoscale parametric simulations and quantitative analyses for designing the shear strength of bar-reinforced UHPFRC beams. The equation considers the contributions of fibre content, shear and flexural reinforcement ratios, and the shear span-to-depth ratio. Its improvement over the AFGC shear design equation is demonstrated based on experimental results of 32 beams with various design parameters.

(4) It is shown that the meso-scale models are not only feasible for elucidating the mechanisms underlying beam failure at material scale, but also potential for improving structural designs of the UHPFRC beams.

Acknowledgement

Y Zhang would like to thank the financial support of a full PhD studentship from Coventry University, UK.

Declaration of conflicting interests

The author(s) declared no potential conflicts of interest with respect to the research, authorship, and/or publication of this article.

Funding

The author(s) disclose receipt of the following financial support for the research, authorship, and/or publication of this article: This study is funded by National Natural Science Foundation of China (No. 52173300 and 51974202), Key Research and Development Programme of Hubei Province (No. 2020BAB052) and Sino-German Center for Research Promotion (Mobility Programme No. M-0172).

References

AFGC (2002). Ultra high performance fibre-reinforced concretes. Interim recommendations. Bagneux, France: SETRA.

Ahmad S, Bahij S, Al-Osta M, Adekunle S, Al-Dulaijan S (2019). Shear behavior of ultra-high-performance concrete beams reinforced with high-strength steel bars. *ACI Structural Journal* 116: 3-14.

Aitcin PC (2000). Cement of yesterday and today-Concrete of tomorrow. *Cement and Concrete Research* 30(9): 1349-1359.

Alberti MG, Enfedaque A, Galvez JC, Canovas MF, Osorio IR (2014). Polyolefin fiber-reinforced concrete enhanced with steel-hooked fibers in low proportions. *Materials and Design* 60: 57-65.

Baby F, Marchand P, Toutlemonde F (2014). Shear behavior of ultrahigh performance fiber-reinforced concrete beams. I: Experimental investigation. *Journal of Structural Engineering* 140(5): 04013111.

Baby F, Marchand P, Toutlemonde F (2013). Shear behavior of ultra high performance fiber reinforced concrete beams. I: Experimental investigation. *Journal of Structural Engineering* 140(5): 04013112.

Bahij S, Adekunle SK, Al-Osta M, Ahmad S, Al-Dulaijan SU, Rahman M (2017). Numerical investigation of the shear behaviour of reinforced ultra-high-performance concrete beams. *Structure Concrete* 19: 305-317.

Barnett SJ, Lataste JF, Parry T, Millard SG, Soutsos MN (2010). Assessment of fibre orientation in ultra high performance fibre reinforced concrete and its effect on flexural strength. *Material Structure* 43(7): 1009-1023.

Bertram G, Hegger J (2012). Shear behvior of pretensioned UHPC beams-Tests and design. Kassel, In Proceddings of the third international symposium on UHPC and nanotechnology for high performance construction materials.

Birtel V, Mark P (2006). Parameterised finite element modelling of RC beam shear failure, United States, ABAQUS Users' Conference.

Boulekbache B, Hamrat M, Chemrouk M, Amziane S (2010). Flowability of fibre-reinforced concrete and its effect on the mechanical properties of the material. *Construction and Building Materials* 24 (9): 1664-1671.

Cao X, Deng XF, Jin LZ, Fu F, Qian K (2019). Shear capacity of reactive powder concrete beams using high-strength steel reinforcement. Proceedings of the institution of civil engineers-structures and buildings.

Cunha VMCF, Barros JAO, Sena-Cruz JM (2012). A finite element model with discrete embedded elements for fibre reinforced composites, *Computers and Structures* 94-94: 22-33.

Dancygier AN, Berkover E (2016). Cracking localization and reduced ductility in fiber-reinforced concrete beams with low reinforcement ratios. *Engineering Structures* 111: 411-424.

Deeb R, Karihaloo BL, Kulasegaram S (2014). Reorientation of short steel fibres during the flow of self-compacting concrete mix and determination of the fibre orientation factor. *Cement and Concrete Research* 56: 112-120.

Earij A, Alfano G, Cashell K, Zhou X (2017). Nonlinear three-dimensional finite element modelling of reinforced-concrete beams: Computational challenges and experimental validation. *Engineering Failure Analysis* 82: 92-115.

Ellis BD, McDowell DL, Zhou M (2014). Simulation of single fiber pullout response with account of fiber morphology. *Cement and Concrete Composites* 48: 42-52

Florent B, Marchand P, Toutlemonde F (2013). Shear behavior of ultrahigh performance fiber-reinforced concrete beams. I: Experimental investigation. *Journal of Structural Engineering* 140: 04013111.

Graybeal BA (2006). Material Property Characterization of Ultra-High Performance Concrete; Publication No. FHWA-HRT-06-United States; Federal Highway Administration, Office of Infrastructure Research and Development: Washington, DC, USA.

Guo ZH (2004). Concrete strength and constitutive relation: Principle and Application. Beijing: China Architecture and Building Press.

Hasgul U, Turker K, Birol T, Yavas A (2018). Flexural behaviour of ultra-high-performance fiber reinforced concrete beams with low and high reinforcement ratios. *Structural Concrete* 19(6): 1577-1590.

Hordijk DA. Tensile and tensile fatigue behaviour of concrete; experiments, modelling and analysis. Heron, 1992, 37: 1-79.

Huang YJ, Yang ZJ, Ren WY, Liu GH, Zhang CH (2015). 3D Meso-scale fracture modelling and validation of concrete based on in-situ X-ray computed tomography images using damage plasticity model. *International Journal of Solids and Structures* 67-68: 340-352.

Huang YJ, Yang YJ, Chen WX, Liu GH (2016). Monte Carlo simulations of meso-scale dynamic compressive behavior of concrete based on X-ray computed tomography images. *International Journal of Impact Engineering* 97: 102-115.

Jia Y, Chen Z, Yan W (2015). A numerical study on carbon nanotube pullout to understand its bridging effect in carbon nanotube reinforced composites. *Composites Part B: Engineering* 81: 64-71.

Kang J, Kim K, Lim YM, Bolander JE (2014). Modeling of fiber-reinforced cement composites: discrete representation of fiber pullout. *International Journal of Solids and Structures* 51: 1970-1979.

Khuntisa M, Stojadinovic B, Goel S (1999). Shear strength of normal and high-strength fiber reinforced concrete beams without stirrups. *ACI Structural Journal* 96(2): 282-289.

Kodur V, Solhmirzaei R, Agrawal A, Aziz EM, Soroushian P (2018). Analysis of flexural and shear resistance of ultra high performance fiber reinforced concrete beams without stirrups. *Engineering Structures* 174: 873-884.

Kwak YK, Eberhard MO, Kim WS, Kim JB (2002). Shear strength of steel fiber-reinforced concrete beams without stirrups. *ACI Structural Journal* 99(4): 530-538.

Laranjeira F, Aguado A, Molins C (2010). Predicting the pullout response of inclined straight steel fibres. *Materials and Structures* 43: 875-895.

Lee J, Fenves GL (1998). Plastic-damage model for cyclic loading of concrete structures. *Journal of Engineering Mechanics* 124(8): 892-900.

Liu H, Xiang T, Zhao R (2009). Research on non-linear structural behaviors of prestressed concrete beams made of high strength and steel fiber reinforced concretes. *Construction and Building Materials* 23: 85-95.

Lim WY, Hong SG (2016). Shear Tests for Ultra-High Performance Fiber Reinforced Concrete (UHPFRC) Beams with Shear Reinforcement. *International Journal of Concrete Structures and Materials* 10(2): 177-188.

Lu C, Leung CKY, Li VC (2017). Numerical model on the stress field and multiple cracking behavior of Engineered Cementitious Composites (ECC). *Construction and Building Materials* 133: 118-127.

Mahmud GH, Yang ZJ, Hassan AMT (2013). Experimental and numerical studies of size effects of Ultra High Performance Steel Fibre Reinforced Concrete (UHPFRC) beams. *Construction and Building Materials* 48: 1027-1034.

Meda A, Minelli F, Plizzari GA (2012). Flexural behaviour of RC beams in fibre reinforced concrete. *Composites: Part B* 43: 2930-2937.

Narayanan R, Darwish IYS (1987). Use of steel fibres as shear reinforcement. *ACI Structural Journal* 84(3): 216-227.

Özcan DM, Bayraktar A, Sahin A, Haktanir T, Turker T (2009). Experimental and finite element analysis on the steel fiber-reinforced concrete (SFRC) beams ultimate behavior. *Construction and Building Materials* 23: 1064-1077.

Pourbaba M, Joghataie A, Mirmiran A (2018). Shear behavior of ultra-high performance concrete. *Construction and Building Materials* 183: 554-564.

Pourbaba M, Sadaghian H, Mirmiran A (2019). A comparative study of flexural and shear behavior of ultra-high-performance fiber-reinforced concrete beams. *Advances of Structural Engineering* 22(7): 1727-1738.

Pros A, Diez P, Molins C (2012). Modeling steel fiber reinforced concrete: numerical immersed boundary approach and a phenomenological mesomodel for concrete-fiber interaction, *International Journal for Numerical Methods in Engineering* 90(1): 65-86.

Pujadas P, Blanco A, Cavalaro SHP, Aguado A, Grunewald S, Blom K, Walraven JC (2014). Plastic fibres as the only reinforcement for flat suspended slabs: parametric study and design considerations. *Construction and Building Materials* 70: 88-96.

Qing L, Yu K, Mu R, Forth JP (2019). Uniaxial tensile behavior of aligned steel fibre reinforced cementitious composites. *Materials and Structures* 52-70.

Qsymah A, Sharma R, Yang Z, Margetts L, Mummery P (2017). Micro X-ray computed tomography image-based two-scale homogenisation of ultra high performance fibre reinforced concrete. *Construction and Building Materials* 130: 230-240.

Richard P, Cheyrezy M (1995). Composition of reactive powder concretes. *Cement and Concrete Research* 25 (7): 1501-1511.

Ridha MMS, Sarsam KF, Al-Shaarbaf IAS (2018). Experimental Study and Shear Strength Prediction for Reactive Powder Concrete Beams. *Case Studies in Construction Materials* 8: 434-446.

Russell HG, Graybeal BA (2013). Ultra-High Performance Concrete: A State-of-the-Art Report for the Bridge Community. Federal Highway Administration, McLean.

Serna P, Arango S, Ribeiro T, Nunez AM, Garcia TE (2009). Structural cast-in-place SFRC: technology, control criteria and recent applications in Spain. *Materials and Structures* 42(9): 1233-1246.

Sharma AK (1986). Shear strength of steel fiber reinforced concrete beams. *ACI Journal* 83(4): 624-628.

Son J, Beak B, Choi C (2011). Experimental study on shear strength for ultra-high performance concrete beam. Proceedings of the 18th International Conference on Composites Materials (ICCM-18).

Tadepalli PR, Dhonde HB, Mo YL, Hsu TT (2015). Shear strength of prestressed steel fiber concrete I-beams. *International Journal of Concrete Structures and Mateirals* 9(3): 267-281.

Taylor HPJ (1969). Investigation of the dowel shear forces carried by the tensile steel in reinforced concrete beams, London: Cement and Concrete Association.

Turker K, Hasgul U, Birol T, Yavas A, Yazici H (2019). Hybrid fiber use on flexural behaviour of ultra high performance fiber reinforced concrete beams. *Composite Structures* 229: 111400.

Voo YL, Poon WK, Foster SJ (2010). Shear strength of steel fiber-reinforced ultrahigh-performance concrete beams without stirrups. *Journal of Structural Engineering* 136(11): 1393–1400.

Voort TV, Suleiman M, Sritharan S (2008). Design and Performance Verification of Ultra-High Performance Concrete Piles for Deep Foundationlowa State University.

Wahba K, Marzouk H, Dawood N (2012). Structural Behavior of UHPFRC Beams without Stirrups. Alberta, 3rd International Structural Specialty Conference.

Wang Q, Song HL, Lu CL, Jin LZ (2020). Shear performance of reinforced ultra-high performance concrete rectangular section beams. *Structures* 27: 1184-1194.

Yang ZJ, Chen J (2005). Finite element modelling of multiple cohesive discrete crack propagation in reinforced concrete beams. *Engineering Fracture Mechanics* 72(14): 2280-2297.

Yang IH, Joh C, Kim BS (2010). Structrual behaviour of ultra high performance concrete beams subjected to bending. *Engineering Structures* 32: 3478-3487.

Yang ZJ, Qsymah A, Peng YZ, Margetts L, Sharma R (2020). 4D characterization of damage and fracture mechanisms of ultra-high performance fibre reinforced concrete by in-situ X-ray computed tomography tests. *Cement and Concrete Composites* 106: 103-437.

Yavaş A, Hasgul U, Turker K, Birol T (2019). Effective fibre type investigation on the shear behavior of ultrahigh-performance fiber-reinforced concrete beams. *Advances in Structural Engineering* 22: 1591-1605.

Yoo DY, Yoon YS (2015). Structural performance of ultra-high-performance concrete beams with different steel fibers. *Engineering Structures* 102(1): 409-423.

Yu RC, Cifuentes H, Rivero I, Ruiz G, Zhang X (2016). Dynamic fracture behaviour in fibre-reinforced cementitious composites, *Journal of the Mechanics and Physics of Solids* 93: 135-152.

Zarrinpour MR, Chao SH (2017). Shear strength enhancement mechanisms of steel fiber-reinforced concrete slender beams. *ACI Structural Journal* 114(3): 729-742.

Zhan Y, Meschke G (2016). Multilevel Computational Model for Failure Analysis of Steel-Fiber-Reinforced Concrete Structures. *Journal of Engineering Mechanics* 04016090.

Zhang H, Huang YJ, Yang ZJ, Xu SL, Chen XW (2018). A discrete-continuum coupled finite element modelling approach for fibre reinforced concrete. *Cement and Concrete Research* 106: 130-143.

Zhang H, Huang YJ, Lin M, Yang ZJ (2022). Effects of fibre orientation on tensile properties of ultra high performance fibre reinforced concrete based on meso-scale Monte Carlo simulations. *Compsite Structures* 287(1): 115331.

Zhang H, Yu RC (2016). Inclined fiber pullout from a cementitious matrix: a numerical study. *Materials* 9(10): 800.

Zhang X, Yang ZJ, Pang M, Yao Y, Li QM, Marrow TJ (2021). Ex-situ micro X-ray computed tomography tests and image-based simulation of UHPFRC beams under bending. *Cement and Concrete Composites* 123: 104216.

Table 1 Material properties of the three-point bending beam (Lim and Hong, 2016)

Property	Matrix	Steel fibres	Steel-bar	Fibre-matrix interface	Steel bar-matrix interface
Elastic modulus E (GPa)	41	200	200	-	-
Poisson ratio v	0.22	0.3	0.3	-	-
Mass density ρ (kg/m^3)	2100	7850	7850	2100	2100
Yield strength f_y (MPa)	-	2500	600	-	-
Ultimate strength f_b (MPa)	-	2800	618	-	-
Ultimate strain ε_u	-	0.1	0.1	-	-
Compressive strength f_c (MPa)	140	-	-	-	-
Tensile strength f_t (MPa)	7	-	-	-	-
Diameter D_f (mm)	-	0.2	29	-	-
Length L_f (mm)	-	16-18	-	-	-
t_{s0} (MPa)	-	-	-	11	15

Table 2 Material properties of the three UHPFRC beams (Bahij et al., 2017)

Property	Matrix	Steel fibre	Steel-bar	Stirrup	Fibre-matrix interface	Steel bar-matrix interface
Elastic Modulus E (GPa)	45	200	200	200	-	-
Poisson ratio v	0.19	0.3	0.3	0.3	-	-
Mass density ρ (kg/m^3)	2450	7850	7850	7850	2100	2100
Yield strength f_y (MPa)	-	2500	1160	430	-	-
Ultimate strength f_b (MPa)	-	2800	1320	540	-	-
Ultimate strain ε_u	-	0.1	0.1	0.1	-	-
Compressive strength f_c (MPa)	120	-	-	-	-	-
Tensile strength f_t (MPa)	5	-	-	-	-	-
Diameter D_f (mm)	-	0.22	15	10	-	-
Length L_f (mm)	-	13	-	-	-	-
t_{s0} (MPa)	-	-	-	-	10	15

Table 3 Material properties of the 32 UHPFRC beams tested by different groups.

References	A_f (%)	ρ_{sv} (%)	*a/d*	*b* (mm)	*d* (mm)	ρ (%)
Pourbaba et al., 2018 (Ref-1)	2.0	0	0.9, 1.2	102, 152	152, 203	2.2-7.8
Wang et al., 2020 (Ref-2)	2.0	0-0.45	1.75-3.0	150	225	6.58
Lim and Hong, 2016 (Ref-3)	1.5	0-0.9	2.68	150	290	7.8
Ahmad et al., 2019 (Ref -4)	1.0, 2.0	0.28, 0.35	1.8	150	228	1.9
Kodur et al., 2018 (Ref-5)	1.5	0	1.6	180	235	0.9, 2.5
Wahba et al., 2012 (Ref-6)	2.0	0	2.3	178	265	1.2, 2.5
Ridha et al., 2018 (Ref-7)	0.5-2.0	0	3.5	100	112	3.4
Yavaş, et al., 2019 (Ref-8)	0.5, 1.0	0	4.0	100	124	5.0
Cao et al., 2019 (Ref-9)	2.0	0-0.58	2.25	150	250	6.58
Son et al., 2011(Ref-10)	2.0	0	2.0	200	300	3.5

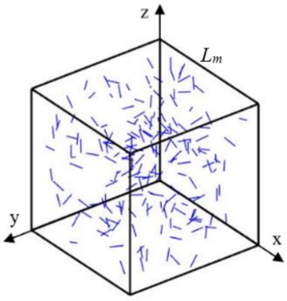

(a) N fibres of length L_f generated in 3D

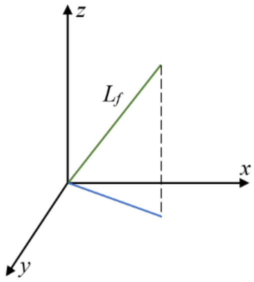

(b) Projecting a fibre in 3D to 2D

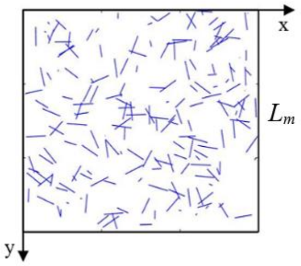

(c) The projected N fibres in the 2D plane

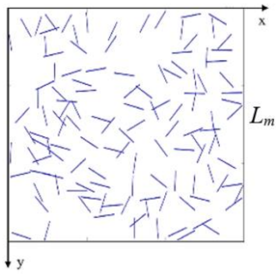

(d) The projected N fibres is modified to N_{2D} fibres based on their length L_f used in 2D models

Figure 1. Projection of fibres in 2D from 3D

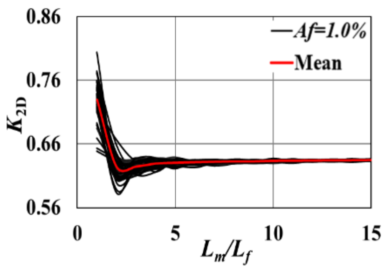

(a) K_{2D} of 750 samples for A_f=1.0%

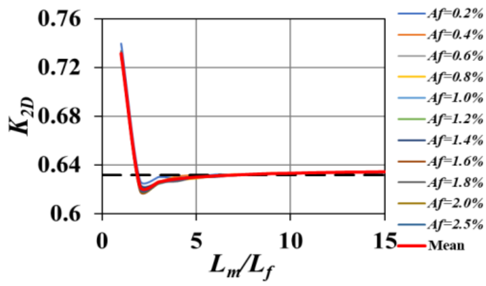

(b) Mean K_{2D} of the 9000 samples with different A_f

Figure 2. Change in K_{2D} of 750 samples with normalized cube size L_m/L_f when A_f=10%(a), change in mean K2D of the 9000 samples with normalized cube size for different A_f (b).

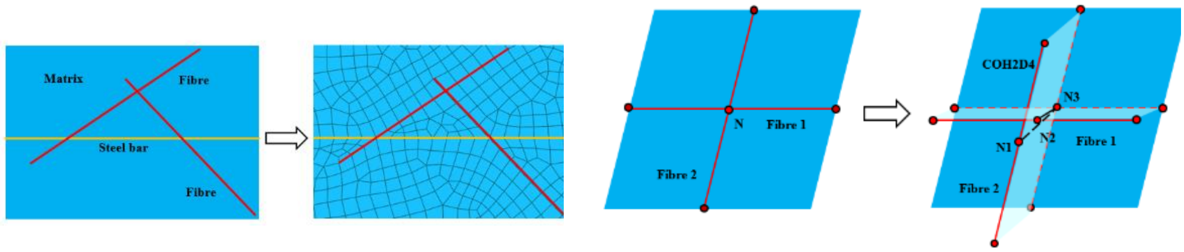

(a) Mesh generation (b) Insertion of cohesive elements

Figure 3. Generation of FE meshes

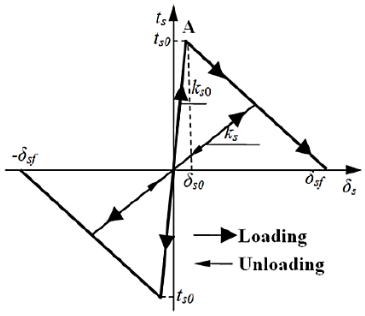

Figure 4. Linear softening bond-slip law for the cohesive elements to model the interface

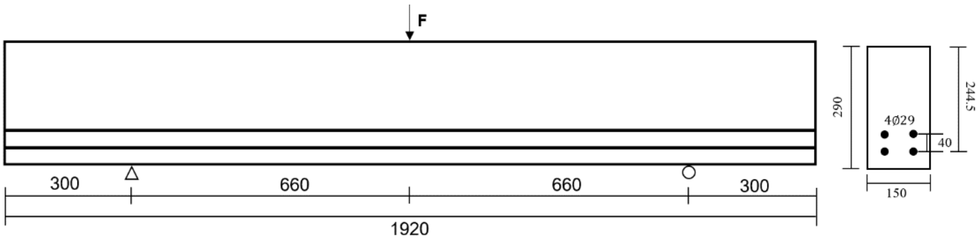

Figure 5. Boundary conditions and geometries of the three-point bending beam

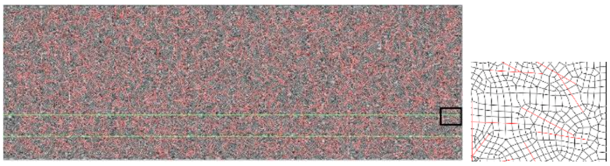

(a) Coarse mesh (elemental size =2mm)

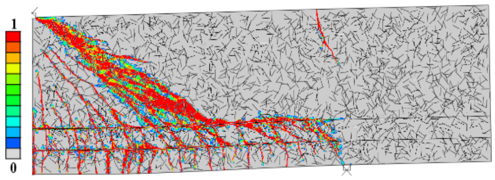

(d) Crack pattern (Coarse mesh)

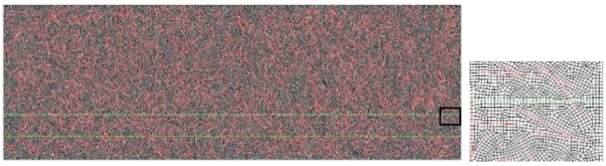

(b) Medium mesh (elemental size=1mm)

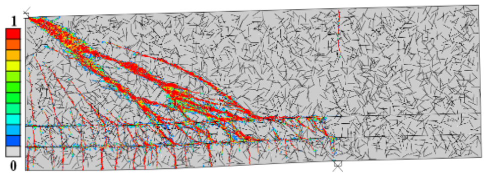

(e) Crack pattern (Medium mesh)

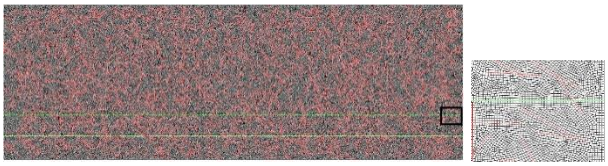

(c) Fine mesh (elemental size =0.75mm)

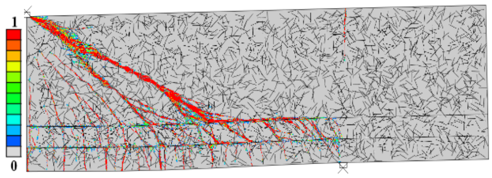

(f) Crack pattern (Fine mesh)

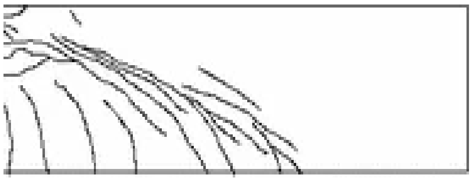

(g) Experimental results (Lim and Hong, 2016)

Figure 6. The three FE meshes (a-c), and the simulated final crack patterns (d-f) for Example 1.

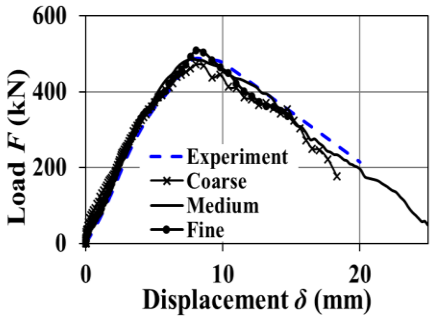

Figure 7. Simulated load (F)-displacement (δ) curves from the three meshes for Example 1.

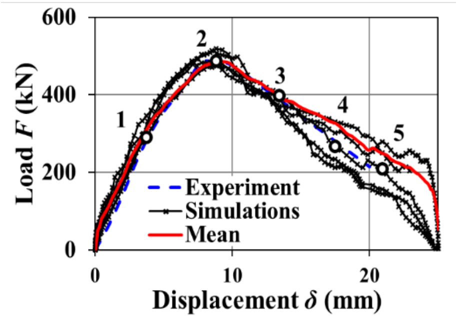

Figure 8. Load (F)-displacement (δ) curves simulated for the five samples in Example 1.

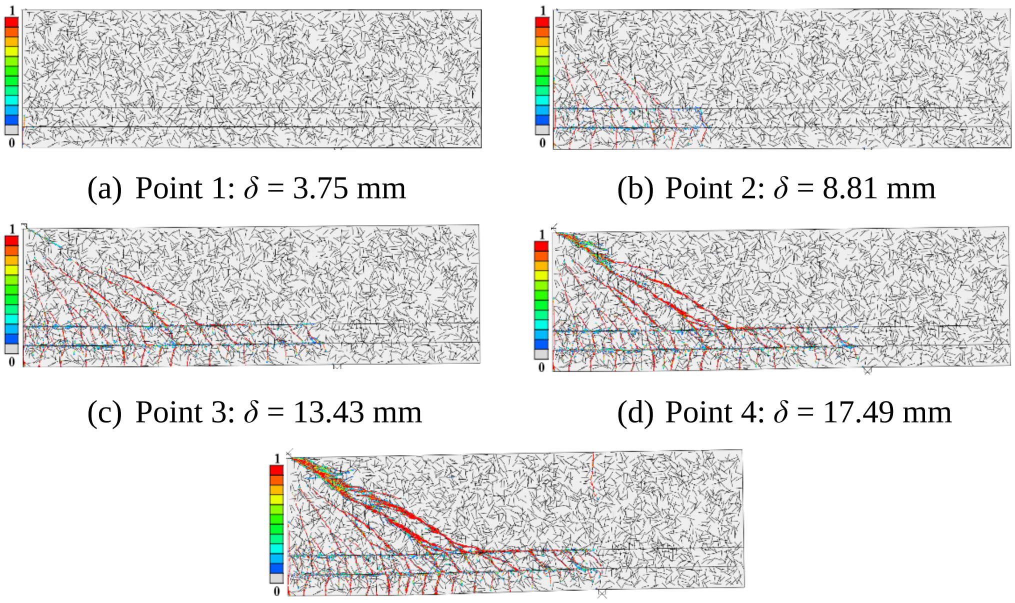

(a) Point 1: δ = 3.75 mm

(b) Point 2: δ = 8.81 mm

(c) Point 3: δ = 13.43 mm

(d) Point 4: δ = 17.49 mm

(e) Point 5: δ = 20.91 mm

Figure 9. Typical cracking process and pattern simulated for Example 1

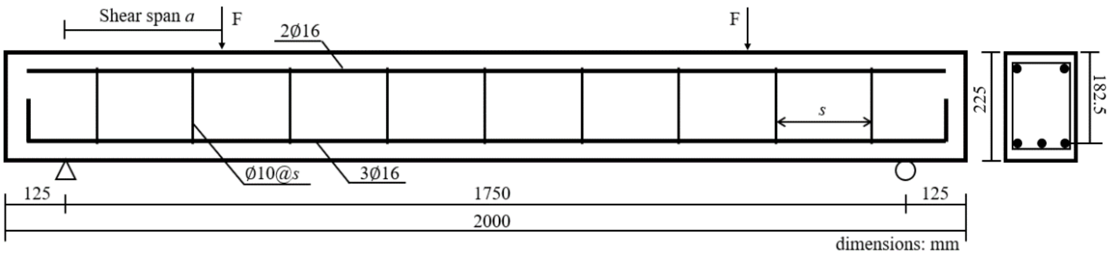

Figure 10. Geometries and boundary conditions for the beams in Example 2

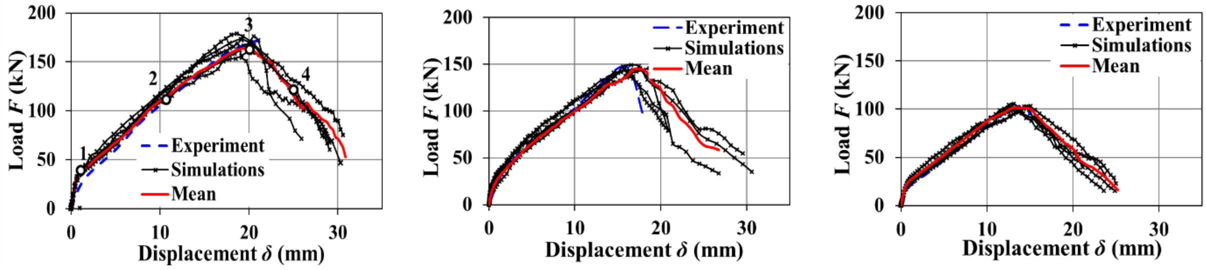

(a) Beam-A (b) Beam-B (c) Beam-C

Figure 11. Simulated shear load-displacement curves in comparison with experimental results for the three beams in Example 2

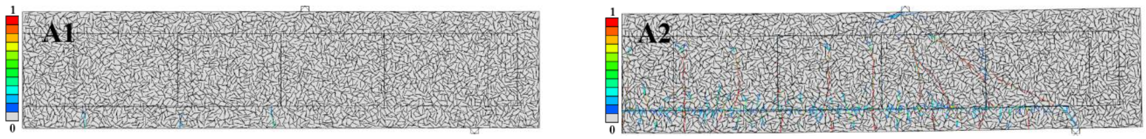

(a) Point 1: δ = 1.31 mm (b) Point 2: δ = 11.22 mm

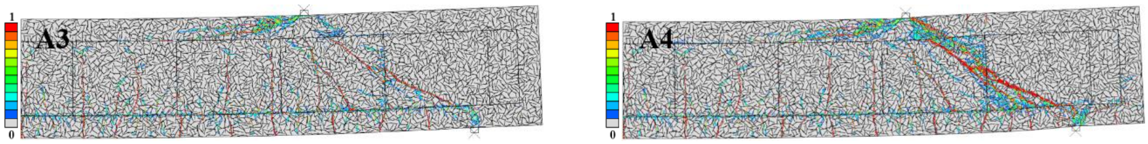

(c) Point 3: δ = 19.29 mm (d) Point 4: δ = 25.20 mm

(e) Experimental results (Bahij et al., 2017)

Figure 12. Simulated cracking process and pattern in comparison with experimental data for Beam-A in Example 2

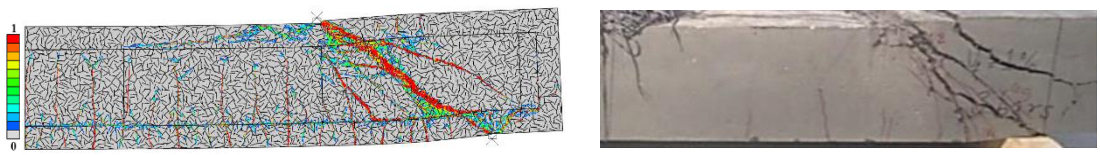

(a) Beam-B

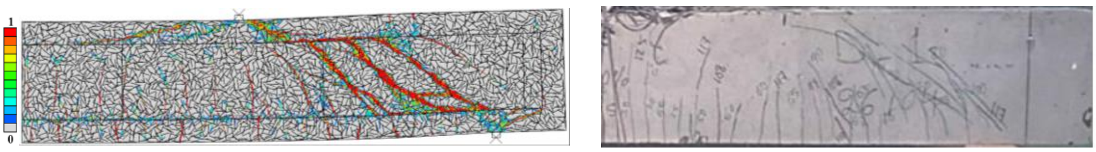

(b) Beam-C

Figure 13. Simulated final crack patterns in comparison with experimental data for Beam-B and Beam-C in Example 2

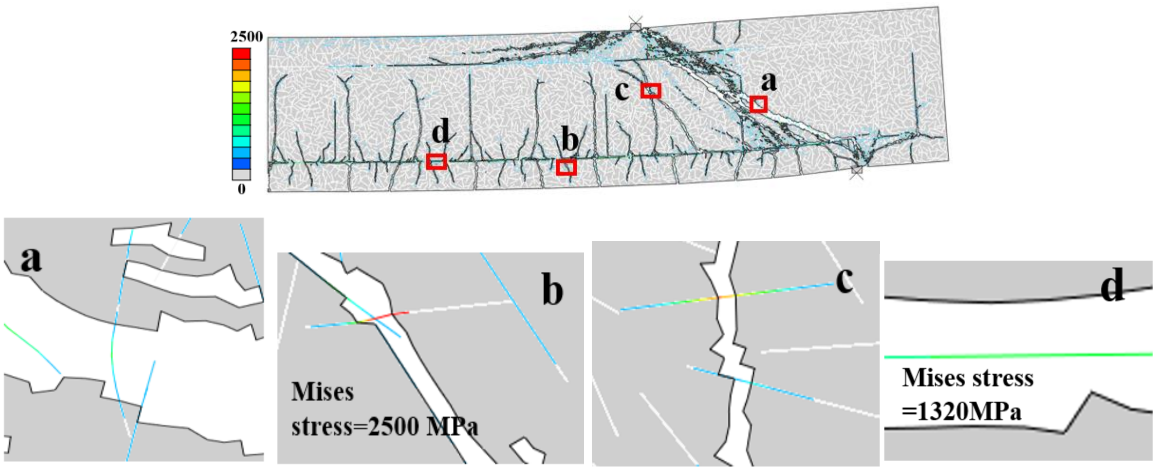

Figure 14. Cut-off views of simulated failure modes (Figure 12d) for Beam-A in Example 2.

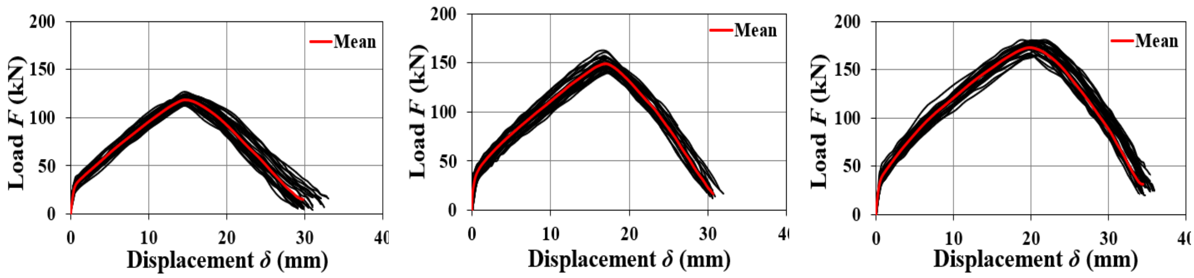

(a) A_f=0.5% (b) A_f=1.0% (c) A_f=1.5%

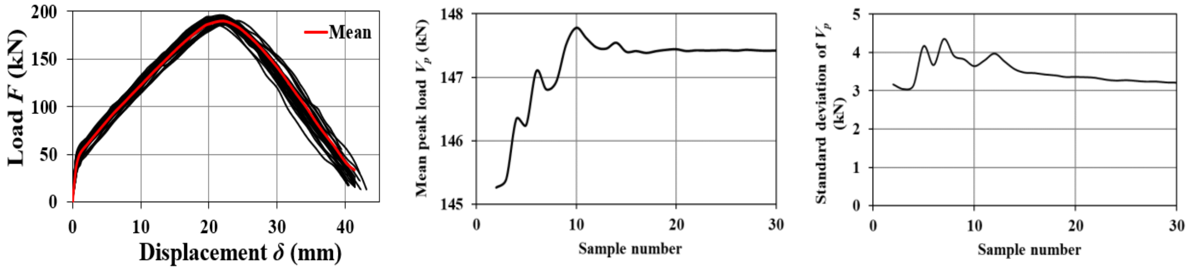

(d) A_f=2.0% (e) Variation in V_p with sample number for A_f=1.0% (f) Standard deviation

Figure 15. The shear load-displacement curve simulated for the 30 samples with different A_f

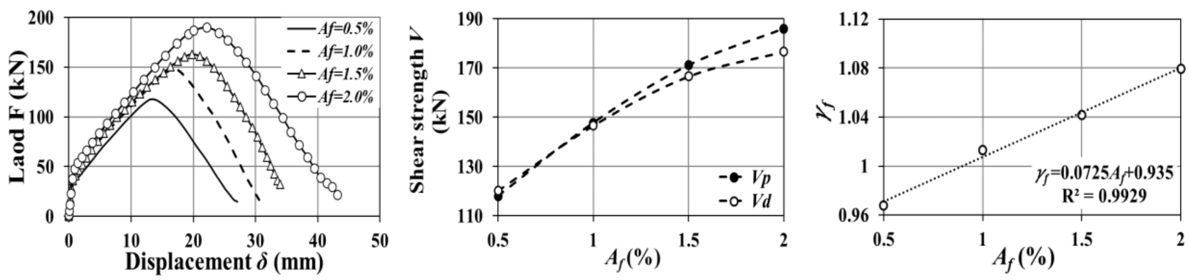

(a) Mean of the 30 samples with different A_f (b) Variation in shear strength with A_f (c) Variation in γ_f with A_f

Figure 16. Change in load with displacement for different A_f (a); changes in the shear strength and the coefficient γ_f with A_f (b, c).

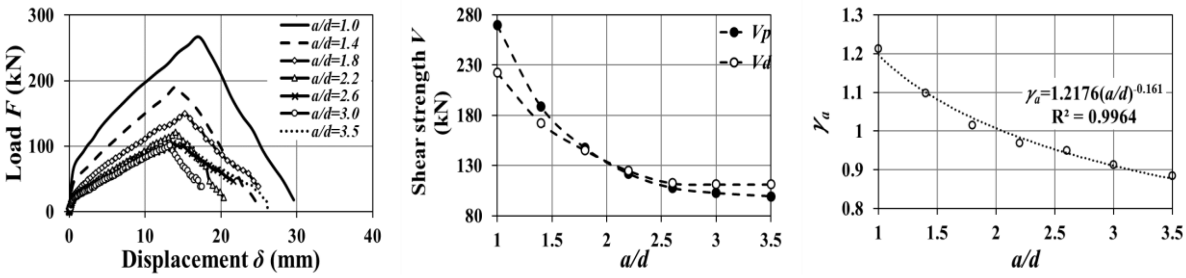

(a) Mean of the 30 samples with different *a/d* (b) Variation in shear strength with *a/d* (c) Variation in γ_a with *a/d*

Figure 17. Change in load with displacement for different *a/d* (a); changes in the shear strength and the coefficient γ_a with *a/d* (b, c).

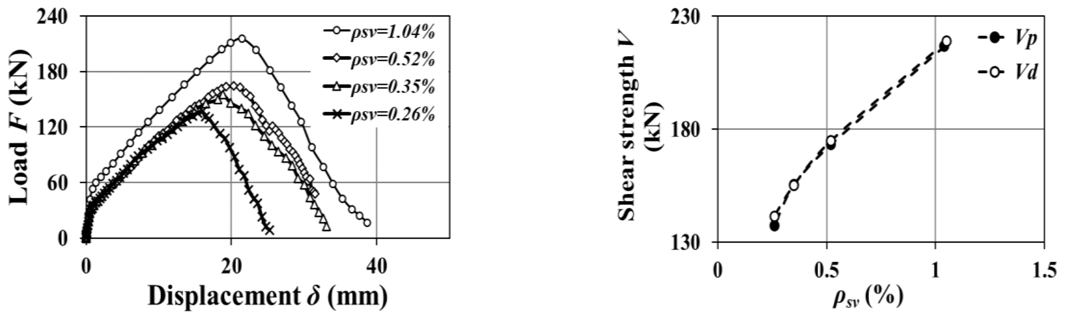

(a) Mean of the 30 samples for different ρ_{sv} (b) Change in shear strength with ρ_{sv}

Figure 18. Change in load and displacement for different ρ_{sv} (a); change in shear strength with ρ_{sv} (b).

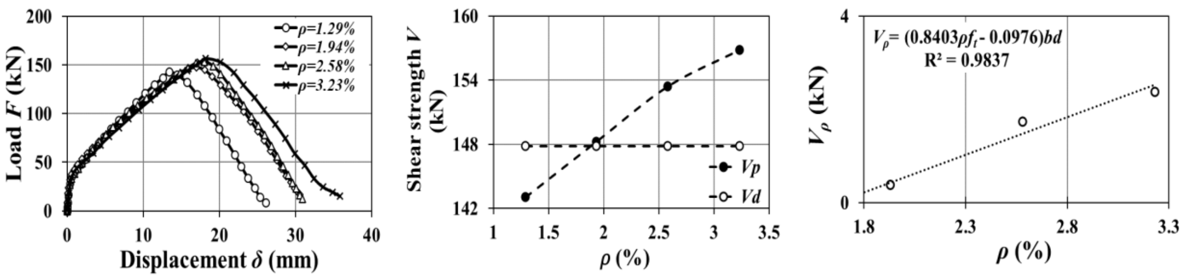

(a) Mean of the 30 samples with different ρ (b) Change in shear strength with ρ (c) Change in V_ρ with ρ

Figure 19. Change in load with displacement for different ρ (a); change in the shear strength and the added term V_ρ with ρ (b, c)

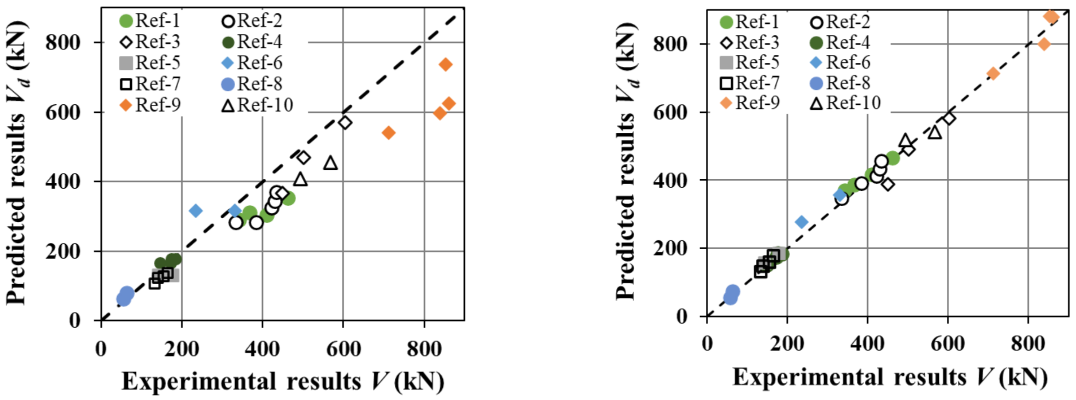

(a) V_d calculated by Eq. 6 compared with experimental results

(b) V_d calculated by Eq. 14 compared with experimental results

Figure 20. Comparison of the predicted shear strength by the AFGC recommended Eq. 6 (a) and the proposed Eq. 14 (b), with experimental data for the 32 beam tests (Table 3)